Physics and Imaging in Radiation Oncology 34 (2025) 100739

Contents lists available at ScienceDirect

Physics and Imaging in Radiation Oncology

journal homepage: www.sciencedirect.com/journal/physics-and-imaging-in-radiation-oncology

Original Research Article

Respiratory navigator-guided multi-slice free-breathing cardiac T_1 mapping on a magnetic resonance-guided linear accelerator☆

Beau P. Pontré [a,b,*], Stefano Mandija [b,c], Manon M.N. Aubert [b], Tim Schakel [b,c], Osman Akdag [b], Katrinus Keijnemans [b], Pim T.S. Borman [b], Astrid L.H.M.W. van Lier [b], Cornelis A.T. van den Berg [b,c], Martin F. Fast [b]

[a] University of Auckland, Department of Anatomy and Medical Imaging, Auckland, New Zealand
[b] University Medical Center Utrecht, Department of Radiotherapy, Utrecht, the Netherlands
[c] University Medical Center Utrecht, Computational Imaging Group for MR Diagnostics and Therapy, Image Sciences Institute, Utrecht, the Netherlands

ARTICLE INFO

Keywords:
Cardiac radioablation
Cardiac T1 mapping
MR-linac

ABSTRACT

Background and Purpose: Image-guided cardiac radioablation on a magnetic resonance-guided linear accelerator (MR-linac) is emerging as a non-invasive treatment alternative for patients with cardiac arrhythmia. Precise target identification is required for such treatments. However, owing to concerns with the use of gadolinium-based contrast agents during treatment with high-energy radiation, non-contrast alternatives must be considered. Native T_1 mapping is a promising technique to delineate myocardial scar which can serve as a surrogate for the treatment target. Further, the likely presence of an implantable cardioverter defibrillator (ICD) in arrhythmia patients necessitates approaches that are robust to metal-related artefacts.

Materials and Methods: We implemented an electrocardiogram (ECG)-triggered free-breathing cardiac T_1 mapping approach on an MR-linac, making use of a respiratory navigator to account for respiratory motion. The technique was validated in a motion phantom and tested in healthy volunteers. We also compared the use of different readout schemes to evaluate performance in the presence of an ICD.

Results: The free-breathing cardiac T_1 mapping approach agreed within 5% compared with ground truth T_1 in a motion phantom. In healthy volunteers, an average difference in T_1 of −3.5% was seen between the free-breathing and breath-hold approaches, but T_1 quantification was impacted by data discarded by the respiratory navigator. Compared to balanced SSFP, the spoiled gradient echo readout was much less susceptible to artefacts caused by an ICD, but the lower signal adversely affected T_1 quantification.

Conclusions: Free-breathing cardiac T_1 mapping is feasible on an MR-linac. Further optimisation is required to reduce scan times and improve accuracy.

1. Introduction

Stereotactic arrhythmia radioablation (STAR) is emerging as a non-invasive alternative to catheter ablation procedures for treatment of cardiac arrhythmias, such as ventricular tachycardia (VT) [1–4]. At present, STAR is used as a salvage treatment option on patients with VT who have had limited success with other forms of treatment including medication, implantable devices, or catheter ablation [5].

Accurate identification of the treatment target is necessary to maximise outcomes and minimise dose to organs at risk. Catheter ablation procedures locate treatment targets based on surface measurements of electrical properties [6]. In STAR, direct electrical measurements are infeasible, so image-based target identification is required. Owing to the soft tissue contrast afforded by magnetic resonance imaging (MRI), magnetic resonance-guided linear accelerator (MR-linac) systems can provide image-based guidance for such treatments [7,8], but image-based target identification remains challenging.

Late gadolinium enhancement with MRI is well-established for identifying myocardial scar, which is used to guide identification of the treatment target in STAR. However, owing to potential safety concerns around the repeated use of gadolinium-based contrast agents and their presence during delivery of high-energy radiation, the use of contrast

☆ This article is part of a special issue entitled: 'MR in RT 2024' published in Physics and Imaging in Radiation Oncology.

* Corresponding author.
E-mail address: b.pontre@auckland.ac.nz (B.P. Pontré).

https://doi.org/10.1016/j.phro.2025.100739
Received 30 August 2024; Received in revised form 20 December 2024; Accepted 24 February 2025
Available online 25 February 2025

agents during treatment is still under investigation [9,10]. In response to these concerns, non-contrast techniques that exploit differences in native cardiac T_1 between myocardial scar and healthy myocardium [11] have been developed. Techniques to quantitatively estimate cardiac T_1 are typically based on the modified Look-Locker inversion recovery (MOLLI) approach [12–14]. Cardiac T_1 quantification typically requires a series of breath-hold scans to minimise motion-related artefacts and errors in T_1 quantification. Free-breathing approaches have been explored for use in diagnostic imaging [15,16], but the long reconstruction times and complex k-space trajectories required in many of these methods are not well-suited to the STAR workflow.

Previous work has shown that breath-hold cardiac T_1 mapping is feasible on an MR-linac [17], but additional challenges are present in patients with VT. Aside from the challenge with multiple consecutive breath-holds, patients who are candidates for cardiac radioablation will likely have an implanted cardioverter defibrillator (ICD). ICD's disrupt MRI acquisition with image artefacts being most apparent in balanced steady-state free precession (bSSFP) sequences [18] which are typically used for cardiac T_1 mapping.

The work presented here demonstrates the feasibility of a free-breathing approach to cardiac T_1 quantification on an MR-linac. We also show that the proposed approach is suitable for use as part of the STAR online workflow through validation on a motion phantom and scans on healthy volunteers.

2. Materials and methods

2.1. Pulse sequence

A multi-slice free-breathing ECG-triggered cardiac T_1 mapping sequence was developed for a 1.5 T Unity MR-linac (Elekta AB, Sweden) based on a 5s(3s)3s MOLLI approach [12] with the number of inversion times acquired varying according to heart rate. A 1D respiratory navigator (RNAV) preceding each single-shot readout allowed for retrospective sorting of each acquisition by RNAV position. The pulse sequence used either a single-shot bSSFP or a spoiled gradient recalled echo (GRE) as the readout scheme (Supplementary Fig. S1). Interleaved slice acquisition that maximised temporal distance between adjacent slices allowed for improved recovery of the longitudinal magnetisation between acquisitions.

2.2. Phantom scans

Eight gel-filled tubes (Eurospin TO5) were used to evaluate the accuracy of the free-breathing approach. Images were acquired from five transverse slices using both the bSSFP and GRE readout. A T_1-mapping scan with a bSSFP readout acquired during breath-hold was used as a reference. Five repetitions of each free-breathing scan were performed to account for images rejected by RNAV sorting. Ground truth T_1 of each tube was measured using a single-slice turbo spin-echo inversion recovery (TSE-IR) sequence with TR = 5000 ms, TE = 10 ms, TI = 25/50/100/200/500/1000/2000/4750 ms, acquired on the same MR-linac system.

The tubes were positioned inside two cylindrical inserts themselves positioned in the body oval of the Quasar^{TM} MRI^{4D} Motion Phantom (IBA Quasar) (Supplementary Fig. S2a-c). The top-most tube in the central insert was obliquely oriented to produce apparent motion in the imaging plane. The left-most tube in the central insert was used for RNAV acquisition. To mimic cardiorespiratory motion, the central insert was connected to the motor of the Motion Phantom. The waveform dictating motion of the insert was a superposition of two sinusoidal waves: a 30 mm peak-to-peak amplitude, 10 cycle/min waveform simulating respiratory motion and a 6 mm peak-to-peak amplitude, 72 cycle/min waveform simulating cardiac motion. The R-wave peaks of a synthetic ECG synchronised with the simulated cardiac motion was used to trigger scanner acquisition (Supplementary Fig. S2d) [19].

2.3. Volunteer scans

In vivo feasibility was evaluated in eleven healthy volunteers (7 men, 4 women; mean age: 28 years, range: 24–32 years). Informed consent was obtained from every subject according to institutional guidelines with Local Ethics Committee approval (NL59820.041.17). Images were acquired in five dynamically planned cardiac mid-ventricular short-axis slices using the same three sequences as the phantom scans. The R-wave peaks of an ECG signal from a four-lead wireless monitoring unit was used to trigger acquisition following a delay of 60 %-80 % of the R-R interval to ensure image acquisition during diastole. In the free-breathing scans, the RNAV was placed on the liver dome providing a 1D projection of the lung-liver interface.

The two free-breathing scans were repeated in all volunteers with an ICD (Claria MRI CRT-D Surescan, Medtronic) placed on the left clavicle, with scanning modes set to ensure safety conditions were met. Imaging parameters used for all scans are in Table 1.

2.4. T_1 quantification

T_1 was quantified by performing a least-squares fit to the signal intensity, s, using a three-parameter exponential recovery model

$$s(TI) = A - Be^{-\frac{TI}{T_1^*}} \quad (1)$$

where, $s(TI)$ is the pixel intensity at TI, T_1^* the apparent modified Look-Locker T_1, and T_1 determined from the three fitting parameters A, B, T_1^* with the Look-Locker correction [13]:

$$T_1 = T_1^*\left(\frac{A}{B} - 1\right) \quad (2)$$

Pixel-wise T_1 maps were generated offline using a custom script (Python) to perform RNAV sorting and least-squares fitting. Only magnitude images were available for offline analysis. The polarity of each $s(TI)$ was corrected so that the coefficient of determination (r^2) to Equation (1) was maximised.

In breath-hold sequences, all acquired images were used for T_1 quantification. In free-breathing scans, only images acquired ± 3 mm from end-expiration as determined by the RNAV position were included. The signal for a given inversion time and slice location was calculated as the mean pixel intensity across the repeats after RNAV sorting.

Owing to the removal of any images outside end-expiration, some inversion times were excluded from T_1 quantification. The effect of

Table 1
Imaging parameters used for phantom and volunteer scans with either a balanced steady-state free precession (bSSFP) or spoiled gradient echo (GRE) readout. The number and range of inversion times for each of the volunteer scans is included in Supplementary Table S2.

	bSSFP (Phantom)	bSSFP (Volunteers)	GRE (Phantom)	GRE (Volunteers)
TR (ms)	3.8	3.8	3.0	3.0
TE (ms)	1.8	1.8	1.6	1.6
Flip angle (°)	35	35	10	10
Number of inversion times	8	Variable	8	Variable
Range of inversion times (ms)	220–4220	Variable	200 – 4200	Variable
Image matrix	256 x 256	320 x 320	256 x 256	320 x 320
Field of View (mm^2)	300 x 300	350 x 350	300 x 300	350 x 350
Pixel size (mm^2)	1.2 x 1.2	1.1 x 1.1	1.2 x 1.2	1.1 x 1.1
Slice thickness (mm)	5	5	5	5

excluding inversion times was evaluated using bSSFP images acquired from the three tubes in the central insert of the stationary phantom which had T_1 closest to that expected in myocardial tissue. T_1 was calculated when iteratively removing either one or two inversion times from the analysis. T_1 calculated from this method was compared to the T_1 calculated using all inversion times.

In volunteers, the myocardium was identified by manually drawing regions of interest along the left-ventricular epicardium and endocardium. Additional points were manually drawn identifying the anterior and posterior insertions to the right ventricle, the centre of the left ventricle, and the centre of the interventricular septum. These four points were used to define six mid-cavity segments as defined by the American Heart Association [20]. Mean T_1 for the whole myocardium was used for comparison of the breath-hold and free-breathing approaches. The mean T_1 for each segment was used to evaluate the effect of an ICD during free-breathing scans.

3. Results

3.1. Phantom

The obliquely-oriented tube in the central insert produced apparent motion of up to ± 5 mm in the anterior-posterior direction. The pixel-wise T_1 maps demonstrate the effect of uncompensated motion on T_1 quantification. Without using RNAV sorting, regions at the edges of the tube showed inconsistent T_1 resulting from the inclusion of all images regardless of position. This effect was absent when retrospective RNAV sorting was applied, giving T_1 maps similar to those produced with a stationary phantom (Fig. 1a-c).

Ground truth T_1 for the tubes ranged from 542 – 1196 ms. The T_1 between the breath-hold and free-breathing approaches using the bSSFP readout differed on average by + 1.5 % (range: [-2.1 %, +6.7 %]). Both the breath-hold and free-breathing bSSFP sequences produced T_1 within 5 % of ground truth T_1, as determined by the TSE-IR sequence, in all tubes except the tube with the longest T_1 (=1196 ms). The use of the GRE as a readout scheme gave consistently lower T_1 than the bSSFP sequences, with an average difference of −11.2 % (range: [-16.4 %, −6.1 %]). The coefficient of variation (CV), calculated as the standard deviation/mean, was higher across all tubes when using the GRE vs bSSFP readout (19.3 % vs 6.8 %) (Fig. 1d, Supplementary Table S1).

The use of RNAV sorting resulted in the rejection of images from the T_1 quantification. In the simulated free-breathing scans on the phantom, 28.5 % of all acquired images in the bSSFP scan and 27 % of images in the GRE scan were within the ± 3 mm acceptance window. In cases where all five repetitions for a given slice and inversion time were excluded, that inversion time was not represented in the pixel-wise curve fits. The effect of removing inversion times from the T_1 quantification is demonstrated in Fig. 2. The largest differences were seen when the first inversion time was not present. Removing later inversion times had a smaller influence on the fit, giving T_1 within ± 2.5 % of the T_1 determined using all inversion times.

3.2. Volunteers

As demonstrated in the phantom results, the volunteer scans were also impacted by missing inversion times following RNAV sorting. Acceptance rates for each individual slice ranged from 7.5 % to 62.5 %. The largest deviations from the T_1 determined by the bSSFP breath-hold sequence was seen at acceptance rates below 20 % (Supplementary Fig. S3).

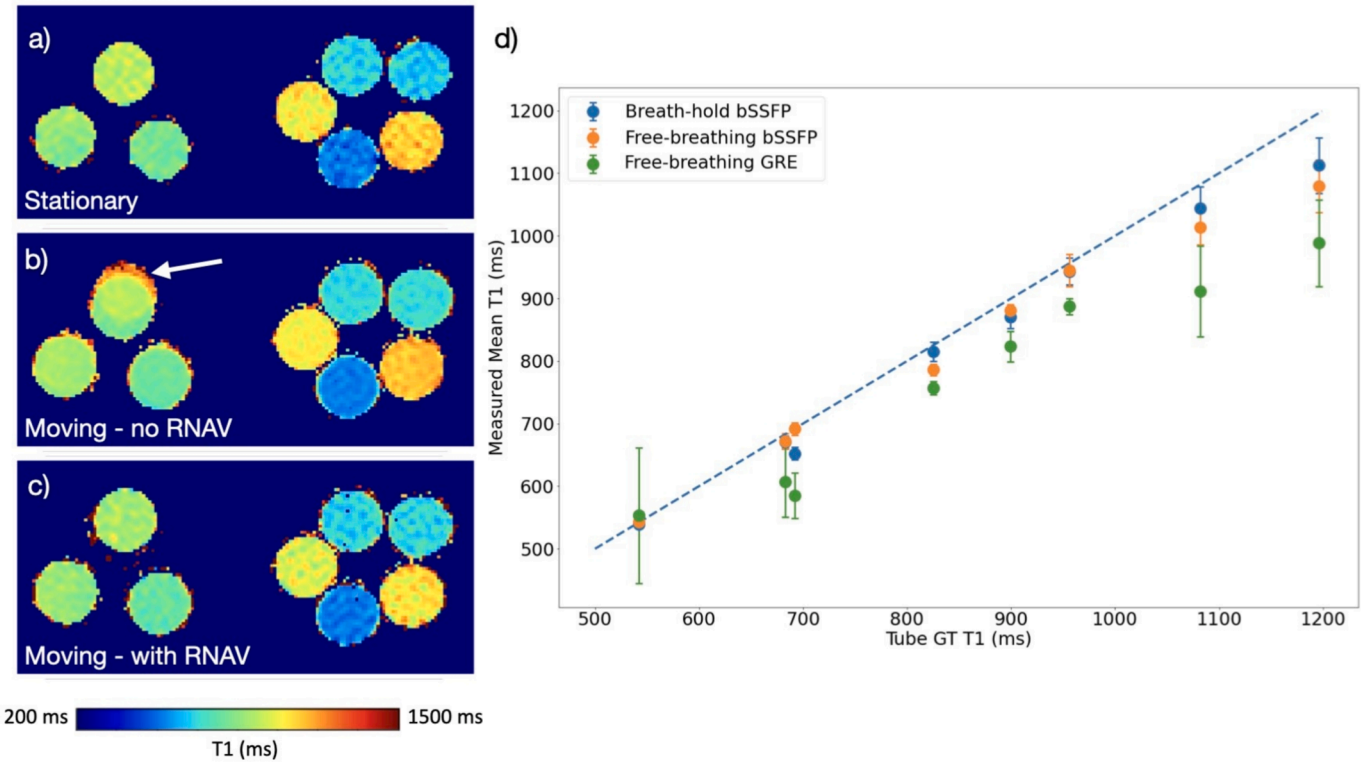

Fig. 1. T_1 maps and comparison of measured T_1 to ground truth for the phantom scans Example pixel-wise T_1 maps from the phantom scans using the balanced steady-state free precession (bSSFP) readout with a) no phantom motion, b) moving central insert with no respiratory navigator (RNAV) sorting and, c) moving central insert with RNAV sorting. The white arrow indicates a typical motion-related artefact that is apparent in the scans without navigator-based sorting and is not visible when the navigator is used. In d), the measured mean T_1 of each tube vs the ground truth (GT) T_1 for the breath-hold bSSFP and free-breathing bSSFP and spoiled GE (GRE) sequences are shown. The dashed line indicates the line of equality with the ground truth measurement. The error bars represent the standard deviation on the mean pixel-wise T_1.

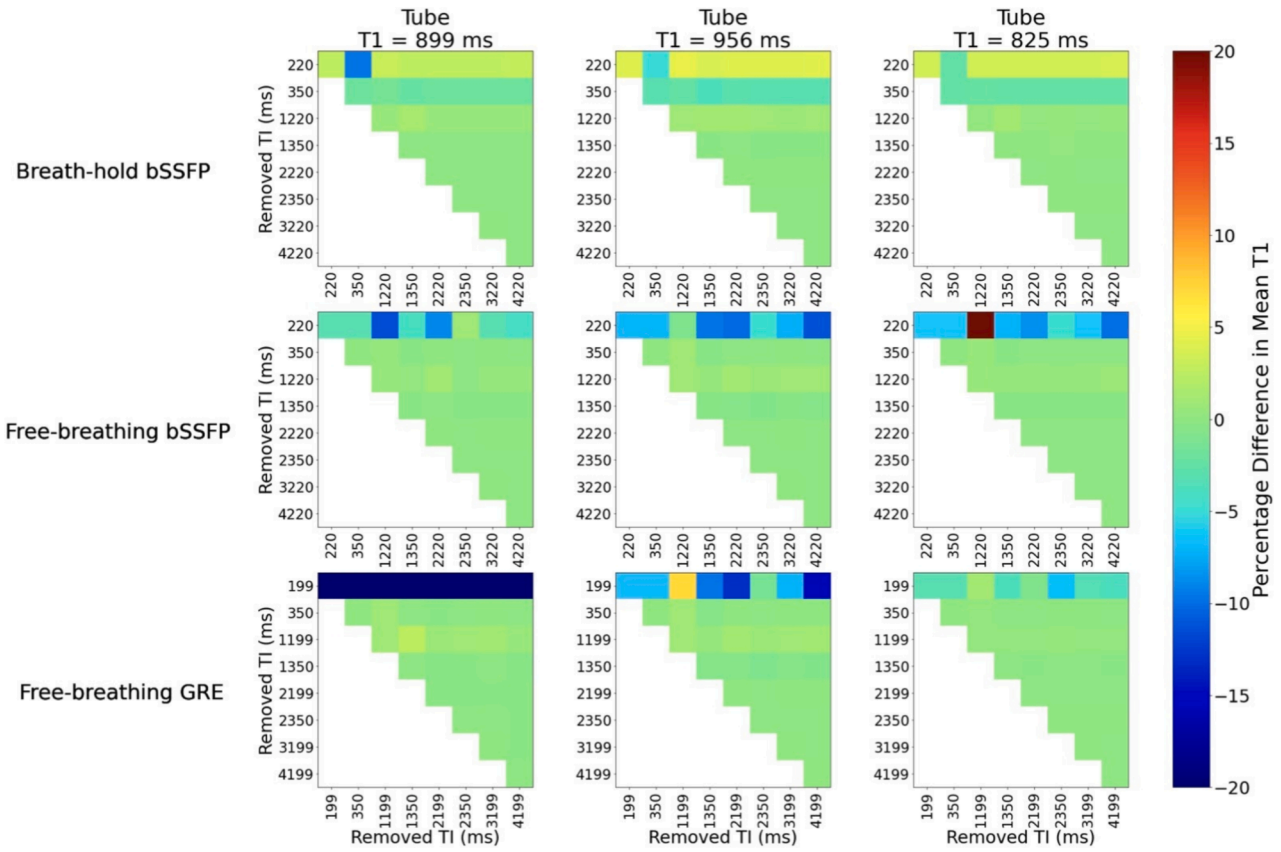

Fig. 2. Heat maps showing the effect of removing inversion times Effect of removing selected inversion times from the analysis for the breath-hold balanced SSFP (bSSFP) and free-breathing bSSFP and spoiled GE (GRE). Each heat map shows the difference from the T_1 estimate using all eight inversion times (TI) compared to removing up to two inversion times. The values along the main diagonal of each grid represents only one missing TI.

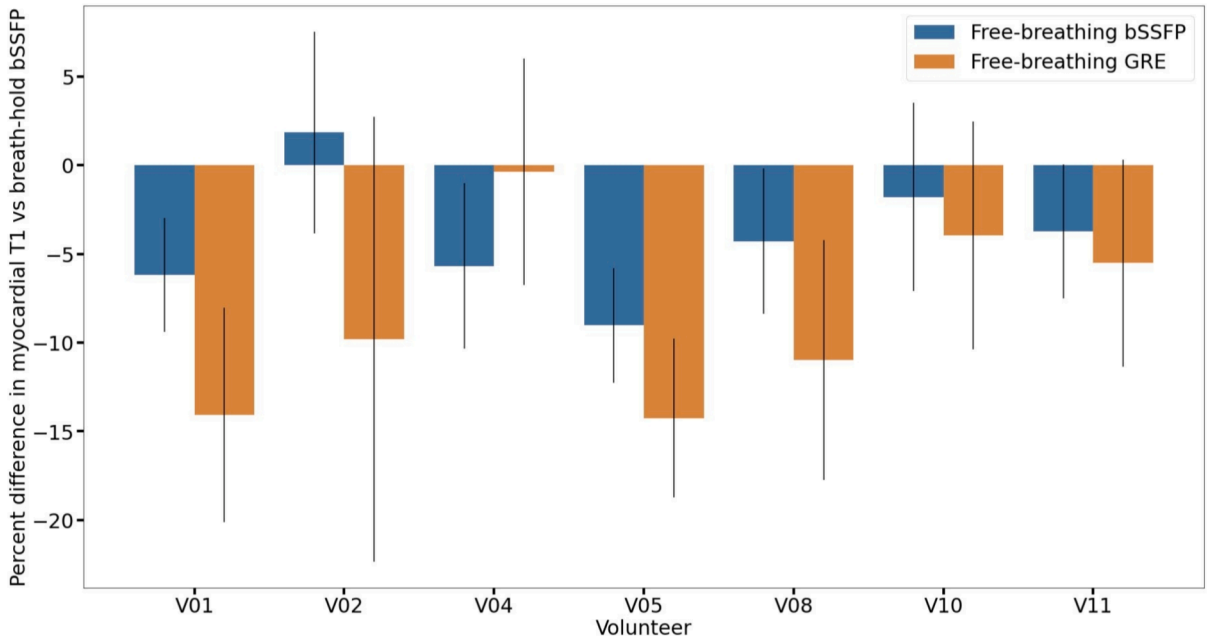

Fig. 3. Percentage difference in mean myocardial T_1 between free-breathing and breath-hold scans on volunteers Percentage difference in mean myocardial T_1 as compared to the T_1 measured by the breath-hold balanced steady-state free precession (bSSFP) sequence for the two free-breathing approaches (bSSFP and spoiled gradient echo (GRE)). Error bars indicate standard deviation. Each value represents the mean over all slices for the volunteers that had the first two inversion times present and had an acceptance rate over 20%. Volunteers V03, V06, V07 and V09 were excluded. Results for all volunteers are provided in Supplementary Table S1.

Scan time for the free-breathing sequences averaged 6:47 min (range: 4:57 min – 8:24 min), varying with heart rate and ECG-gating efficiency. Breath-hold scans required breath-holds of 12–15 s per slice, totalling 60–75 s acquisition for five slices, excluding preparation time between successive breath-holds. Mean myocardial T_1 was generally lower using the free-breathing approach as compared to the mean T_1 determined by the breath-hold bSSFP (Fig. 3). As acceptance rate analyses showed a smaller T_1 difference from the breath-hold T_1 with the first two inversion times present and acceptance rate above 20 %, only slices that met those criteria were included. Applying these criteria eliminated 4 of the 11 volunteers. Across the included volunteers, the change from the breath-hold derived T_1 was −3.5 % when using the free-breathing bSSFP sequence (range: [-9.3 %, 2.6 %]) and −8.5 % with the free-breathing GRE (range: [-14.9 %, 0.4 %]). The difference was not statistically significant ($p = 0.50$, Wilcoxon rank test).

T_1 maps produced from the free-breathing approach were similar in appearance to those acquired during breath-hold. Example from one volunteer shown in Fig. 4. In all volunteers, T_1 maps produced by the bSSFP sequences had a lower mean CV for breath-hold (19.5 %) and free-breathing (18.5 %) as compared to a mean CV of 37.0 % in the free-breathing GRE sequence ($p = 0.015$, Wilcoxon rank test) (Supplementary Table S2).

Without RNAV sorting, tissue interfaces were poorly defined and T_1 quantification became unreliable. Artefacts associated with misregistration of the tissues were seen in both the bSSFP and GRE sequences (Fig. 4c,e). The use of RNAV sorting minimised motion-related artefacts, producing images similar in appearance to the end-exhalation breath-hold scans.

3.3. Effect of ICD

In the presence of an ICD, the bSSFP images showed signal loss and banding related to magnetic field inhomogeneities (Fig. 5). The GRE sequence showed only signal loss in the anterior chest wall and anterior segments of the myocardium. Metal-related artefacts in the raw images impacted pixel-wise T_1 quantification with the bSSFP showing banding artefacts (Fig. 5e). In the GRE sequence, T_1 quantification was minimally impacted by metal-related artefacts. The greatest impact on mean regional T_1 was seen with the bSSFP when the ICD was present, leading to longer mean T_1 in the anterior segment (Fig. 5g).

4. Discussion

In this work, a MOLLI T_1 quantification approach was adapted to allow free-breathing, multi-slice T_1 quantification on a 1.5 T MR-linac. The technique was validated in a motion phantom and results in volunteers demonstrate that this approach is feasible for myocardial T_1 quantification. With scan times under 8 min, and short reconstruction times to produce T_1 maps, the approach would be suitable for online use during STAR treatment planning. While the primary motivation for developing this technique is reliable identification of myocardial scar in patients undergoing STAR, T_1 quantification could have other uses in thoracic radiotherapy, such as the assessment of radiation-induced cardiovascular toxicity [21,22].

To be successful for target identification in STAR, T_1 quantification must be sufficiently precise to distinguish scar from healthy myocardium. MOLLI approaches show higher precision when compared to other methods used for cardiac T_1 mapping [23]. Previous studies in patients with chronic myocardial infarction have shown that myocardial scar has on average a 15 % higher T_1 than healthy myocardium [11]. The free-breathing bSSFP approach produces images with lower T_1 than the breath-hold approach with CV less than 5 %. While absolute T_1 varies between patients, the free-breathing approach will provide sufficient relative T_1 differences in an individual to allow delineation of myocardial scar. For the free-breathing GRE sequence, the CV is much larger, owing to the lower signal-to-noise ratio (SNR) in the acquired image data. In this case, the ability to delineate regions of T_1 resulting from myocardial scarring could be compromised. Further investigation in relevant patient groups is necessary to evaluate clinical utility and sensitivity to relevant pathology.

A multi-slice approach ensures better heart coverage in a single acquisition. However, in both volunteers and phantoms, the calculated T_1 underestimates T_1 measurements made using a breath-hold approach. The breath-hold approach, which uses separate acquisitions for each slice, allows complete recovery of longitudinal magnetisation. The interleaved multi-slice approach used here avoids repeated signal acquisition in individual slices. However, a non-selective inversion pulse is applied at the beginning of each block. The 5s(3s)3s MOLLI scheme

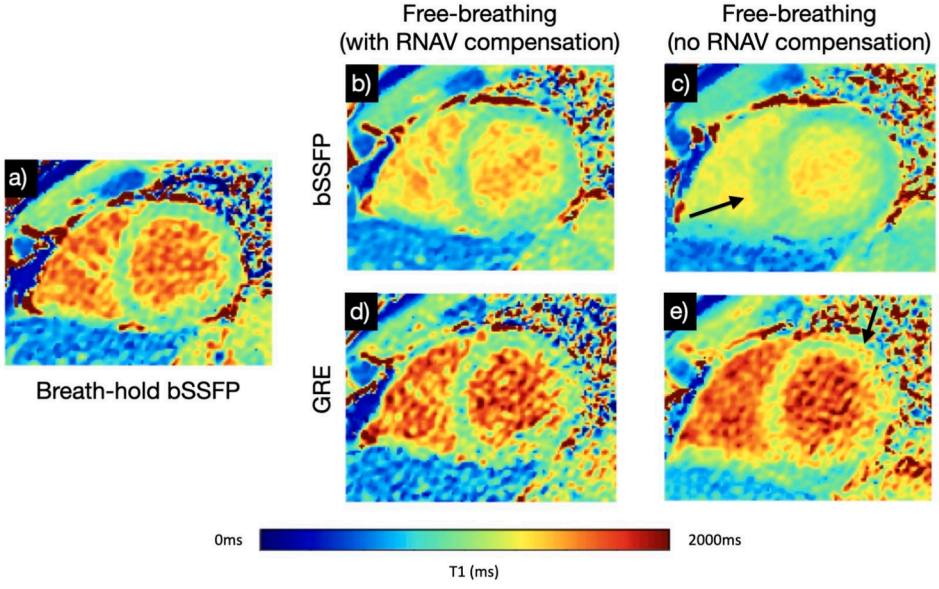

Fig. 4. Example pixel-wise T_1 maps from volunteer scans Example pixel-wise T_1 maps showing the effect of the respiratory navigator (RNAV) sorting in the volunteer scans. a) breath-hold balanced steady-state free precession (bSSFP), b) free-breathing bSSFP with navigator-based sorting, c) free-breathing bSSFP without navigator-based sorting, d) free-breathing spoiled gradient echo (GRE) with navigator-based sorting, e) free-breathing GRE without navigator-based sorting. Arrows on c) and e) demonstrate artefacts related to uncompensated motion.

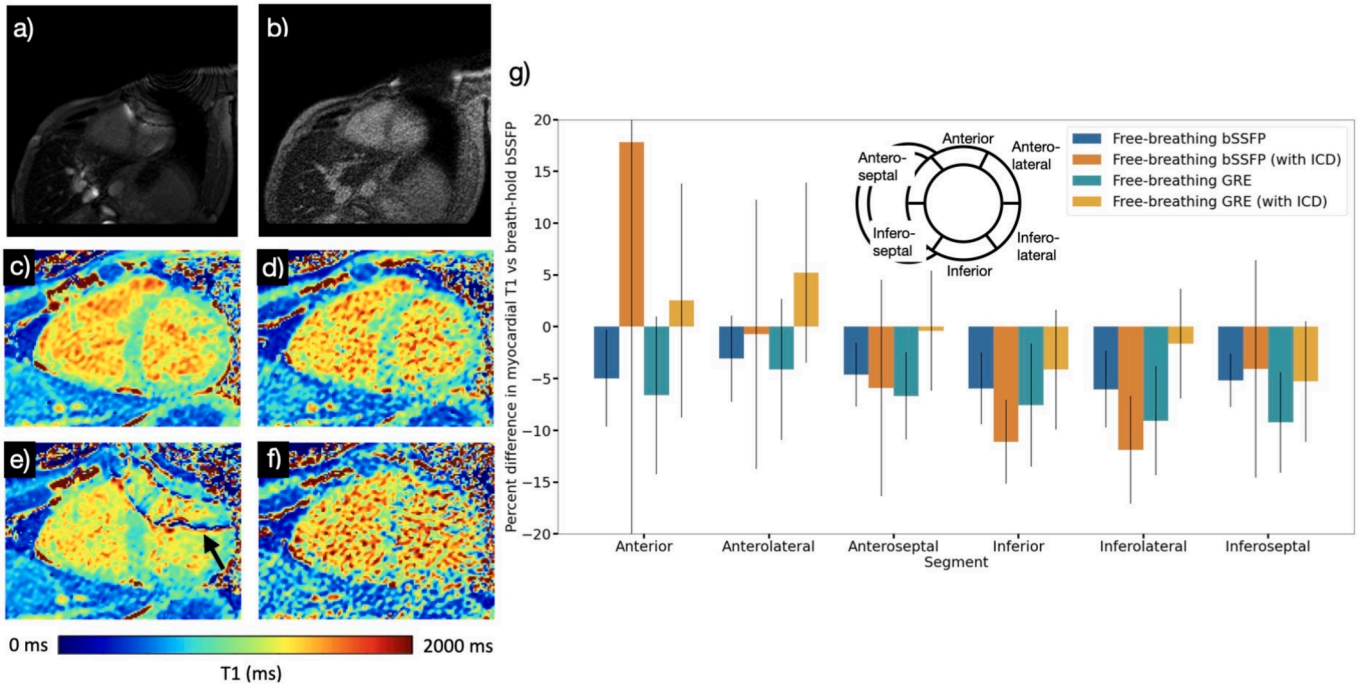

Fig. 5. Example images and T_1 maps with and without ICD, and graph of percent difference in T_1 by mid ventricular segment a) Acquired balanced steady-state free precession (bSSFP) image at TI = 350 ms with implantable cardioverter defibrillator (ICD) present, b) acquired spoiled gradient echo (GRE) image at TI = 350 ms with ICD present. c-f) Example T_1 maps from the free-breathing sequences demonstrating the effect of an ICD placed on the clavicle of the volunteers. c) bSSFP without ICD present d) GRE without ICD present, e) bSSFP with ICD present f) GRE with ICD present. Arrow on e) shows the inhomogeneity artefact caused by the nearby ICD. g) Difference in mean myocardial T_1 as compared to the breath-hold bSSFP sequence by segment for the bSSFP and GRE approach, both with and without an ICD place on the clavicle of the volunteer. The mean percentage difference for each segment represents the average over all volunteers and all slices. Error bars indicate standard deviation. The standard deviation for the anterior segment in the bSSFP with ICD is truncated for display (actual value ± 47.2 %) Inset schematic shows the six segments.

ensures a minimum of three seconds for longitudinal recovery before application of subsequent inversion pulses. Although absolute T_1 quantification may be affected by the shorter recovery time, relative T_1 changes within the myocardium are still apparent.

The 5 mm slice thickness used in this study is smaller than those (8–10 mm) typically used in 2D cardiac T_1 mapping [24–26]. The choice of slice thickness was motivated by the need for higher spatial resolution in STAR to appropriately contour target volumes and minimize dose to healthy myocardium and organs at risk. The reduced signal resulting from smaller voxel sizes is more problematic when using a GRE readout owing to the lower SNR. While the precision of the bSSFP approach may be sufficient, the GRE approach may be infeasible with thinner slices without additional signal averaging. T_1 mapping using 3D acquisition strategies would improve SNR and produce the higher, isotropic resolution required for STAR [15,27]. Methods that combine T_1 with T_2 and other quantitative metrics [27,28], including MR fingerprinting and multitasking approaches [29,30], also show promise for more precise cardiac tissue characterisation, but the long reconstruction times associated with these methods may be incompatible with the online STAR workflow.

Accurate T_1 quantification relies on the number and distribution of inversion times available [31]. The phantom experiments show that T_1 estimation is highly dependent on the presence of the earliest inversion times during signal recovery. The RNAV in the free-breathing approach eliminates acquisitions that are not at end-exhalation. With acceptance rates not exceeding 62.5 %, it is inevitable that some inversion times will be missing from T_1 estimation. In the case of irregular breathing, lower acceptance rates will adversely impact T_1 calculation. The analysis of removed inversion times suggests that beyond the crucial early TIs, removal of up to two TIs does not greatly impact T_1 estimation. Alternative acquisition schemes using fewer TIs, with repetition schemes to maximise RNAV acceptance could improve performance. Scan time could be reduced by exploring alternative motion compensation methods such as non-rigid registration [32] and self-gating [15]. Free-running approaches using radial acquisition can also remove the need for ECG triggering during scans, allowing for improved patient comfort [15]. Providing feedback to patients to assist with breathing more consistently has been shown to reduce breathing variability [33] and could also improve acceptance rates.

Balanced steady-state sequences are typically used as the readout strategy for cardiac T_1 mapping owing to their high signal and contrast. However, bSSFP sequences are highly sensitive to magnetic field inhomogeneities [18]. For this reason, they are typically not suited to imaging in the vicinity of implanted devices and GRE sequences are preferred [34]. Patients undergoing cardiac radioablation, will likely have an ICD present, which will adversely affect T_1 quantification. With the GRE sequence, signal loss was apparent in the anterior segments of the heart resulting in increased T_1. The pixel-wise T_1 maps clearly demonstrate the impact of the inhomogeneity artefacts when using the bSSFP sequence, making target identification challenging in affected areas. Approaches to minimise the impact of field inhomogeneities such as phase cycling [35], alternative sampling strategies [36,37] and machine learning-based post-processing [38] could be employed, although their impact on scan time, and appropriateness for use in the online STAR workflow would need to be considered.

This study represents a first step toward free-breathing cardiac T_1 mapping on an MR-linac but is limited in that it was performed on only a small number of healthy participants. While volunteers were useful to demonstrate technical feasibility, a more substantial study in a patient cohort is needed to evaluate clinical utility. In particular, the present study did not explore the impact of irregular heart rhythm and respiration. Anti-tachycardia pacing and arrhythmia rejection are often used during imaging, but whether these strategies affect T_1 quantification with the proposed approach is not known. Techniques to manage

respiration and maximise acceptance rates in patients with irregular breathing will also need to be explored. Further, while the proposed technique is sensitive to relative T_1 changes, absolute T_1 is underestimated. Whether relative T_1 changes are of use in clinical decision making for STAR will need to be investigated.

In conclusion, the free-breathing cardiac T_1 mapping approaches investigated here are feasible on a 1.5 T MR-linac. They produce T_1 estimates in line with breath-hold techniques and have precision and resolution suited to use for STAR. Further optimisation in acquisition and post-processing is required to reduce scan times, improve accuracy, and ensure robust performance in the presence of ICDs.

CRediT authorship contribution statement

Beau P. Pontré: Conceptualization, Software, Investigation, Writing – original draft. **Stefano Mandija:** Conceptualization, Supervision, Writing – original draft. **Manon M.N. Aubert:** Investigation, Validation, Writing – original draft. **Tim Schakel:** Resources, Software, Writing – review & editing. **Osman Akdag:** Resources. **Katrinus Keijnemans:** Resources, Writing – review & editing. **Pim T.S. Borman:** Resources. **Astrid L.H.M.W. van Lier:** Supervision, Writing – review & editing. **Cornelis A.T. van den Berg:** Resources, Supervision. **Martin F. Fast:** Conceptualization, Funding acquisition, Supervision, Writing – original draft.

Declaration of competing interest

The authors declare that they have no known competing financial interests or personal relationships that could have appeared to influence the work reported in this paper.

Acknowledgements

The authors acknowledge funding by the Dutch Research Council (NWO) through project no. 19484 (MEGAHERTZ) and the Auckland Medical Research Foundation (AMRF) Gavin and Ann Kellaway Medical Research Fellowship project no. 1719003

Appendix A. Supplementary data

Supplementary data to this article can be found online at https://doi.org/10.1016/j.phro.2025.100739.

References

[1] Chin R, Hayase J, Hu P, Cao M, Deng J, Ajijola O, et al. Non-invasive stereotactic body radiation therapy for refractory ventricular arrhythmias: an institutional experience. J Interv Card Electrophysiol 2021;61:535–43. https://doi.org/10.1007/s10840-020-00849-0.

[2] Gianni C, Rivera D, Burkhardt JD, Pollard B, Gardner E, Maguire P, et al. Stereotactic arrhythmia radioablation for refractory scar-related ventricular tachycardia. Heart Rhythm 2020;17:1241–8. https://doi.org/10.1016/j.hrthm.2020.02.036.

[3] Lloyd MS, Wight J, Schneider F, Hoskins M, Attia T, Escott C, et al. Clinical experience of stereotactic body radiation for refractory ventricular tachycardia in advanced heart failure patients. Heart Rhythm 2020;17:415–22. https://doi.org/10.1016/j.hrthm.2019.09.028.

[4] Cuculich PS, Schill MR, Kashani R, Mutic S, Lang A, Cooper D, et al. Noninvasive cardiac radiation for ablation of ventricular tachycardia. N Engl J Med 2017;377:2325–36. https://doi.org/10.1056/NEJMoa1613773.

[5] Neuwirth R, Cvek J, Knybel L, Jiravsky O, Molenda L, Kodaj M, et al. Stereotactic radiosurgery for ablation of ventricular tachycardia. EP Eur 2019;21:1088–95. https://doi.org/10.1093/europace/euz133.

[6] Nakahara S. Catheter ablation of ventricular tachycardia associated with structural heart disease: current status and perspectives. J Cardiol 2023;81:57–62. https://doi.org/10.1016/j.jjcc.2022.09.008.

[7] Mayinger M, Kovacs B, Tanadini-Lang S, Ehrbar S, Wilke L, Chamberlain M, et al. First magnetic resonance imaging-guided cardiac radioablation of sustained ventricular tachycardia. Radiother Oncol 2020;152:203–7. https://doi.org/10.1016/j.radonc.2020.01.008.

[8] Bianchi S, Marchesano D, Magnocavallo M, Polselli M, Di Renzi P, Grimaldi G, et al. Magnetic resonance-guided stereotactic radioablation for septal ventricular tachycardias. JACC Clin Electrophysiol 2024:S2405500X24007497. https://doi.org/10.1016/j.jacep.2024.08.008.

[9] Groot Koerkamp ML, Vasmel JE, Russell NS, Shaitelman SF, Anandadas CN, Currey A, et al. Optimizing MR-guided radiotherapy for breast cancer patients. Front Oncol 2020;10:1107. https://doi.org/10.3389/fonc.2020.01107.

[10] Wang J, Salzillo T, Jiang Y, Mackeyev Y, David Fuller C, Chung C, et al. Stability of MRI contrast agents in high-energy radiation of a 1.5T MR-Linac. Radiother Oncol 2021;161:55–64. https://doi.org/10.1016/j.radonc.2021.05.023.

[11] Messroghli DR, Walters K, Plein S, Sparrow P, Friedrich MG, Ridgway JP, et al. Myocardial T_1 mapping: application to patients with acute and chronic myocardial infarction. Magn Reson Med 2007;58:34–40. https://doi.org/10.1002/mrm.21272.

[12] Kellman P, Arai AE, Xue H. T1 and extracellular volume mapping in the heart: estimation of error maps and the influence of noise on precision. J Cardiovasc Magn Reson 2013;15:56. https://doi.org/10.1186/1532-429X-15-56.

[13] Messroghli DR, Radjenovic A, Kozerke S, Higgins DM, Sivananthan MU, Ridgway JP. Modified Look-Locker inversion recovery (MOLLI) for high-resolution T1 mapping of the heart. Magn Reson Med 2004;52:141–6. https://doi.org/10.1002/mrm.20110.

[14] Piechnik SK, Ferreira VM, Dall'Armellina E, Cochlin LE, Greiser A, Neubauer S, et al. Shortened modified look-locker inversion recovery (ShMOLLI) for clinical myocardial T1-mapping at 1.5 and 3 T within a 9 heartbeat breathhold. J Cardiovasc Magn Reson 2010;12:1–11. https://doi.org/10.1186/1532-429X-12-69.

[15] Qi H, Jaubert O, Bustin A, Cruz G, Chen H, Botnar R, et al. Free-running 3D whole heart myocardial T1 mapping with isotropic spatial resolution. Magn Reson Med 2019;82:1331–42. https://doi.org/10.1002/mrm.27811.

[16] Weingärtner S, Akçakaya M, Roujol S, Basha T, Stehning C, Kissinger KV, et al. Free-breathing post-contrast three-dimensional T1 mapping: volumetric assessment of myocardial T1 values. Magn Reson Med 2015;73:214–22. https://doi.org/10.1002/mrm.25124.

[17] Akdag O, Mandija S, van Lier ALHMW, Borman PTS, Schakel T, Alberts E, et al. Feasibility of cardiac-synchronized quantitative T1 and T2 mapping on a hybrid 1.5 Tesla magnetic resonance imaging and linear accelerator system. Phys Imaging Radiat Oncol 2022;21:153–9. https://doi.org/10.1016/j.phro.2022.02.017.

[18] Scheffler K, Lehnhardt S. Principles and applications of balanced SSFP techniques. Eur Radiol 2003;13:2409–18. https://doi.org/10.1007/s00330-003-1957-x.

[19] Akdag O, Borman PTS, Mandija S, Woodhead PL, Uijtewaal P, Raaymakers BW, et al. Experimental demonstration of real-time cardiac physiology-based radiotherapy gating for improved cardiac radioablation on an MR-linac. Med Phys 2024;51:2354–66. https://doi.org/10.1002/mp.17024.

[20] Cerqueira MD, Weissman NJ, Dilsizian V, Jacobs AK, Kaul S, Laskey WK, et al. Standardized myocardial segmentation and nomenclature for tomographic imaging of the heart. Circulation 2002;105:539–42. https://doi.org/10.1161/hc0402.102975.

[21] Ricco A, Slade A, Canada JM, Grizzard J, Dana F, Rezai Gharai L, et al. Cardiac MRI utilizing late gadolinium enhancement (LGE) and T1 mapping in the detection of radiation induced heart disease. Cardio-Oncol 2020;6:6. https://doi.org/10.1186/s40959-020-00061-z.

[22] Tahir E, Azar M, Shihada S, Seiffert K, Goy Y, Beitzen-Heineke A, et al. Myocardial injury detected by T1 and T2 mapping on CMR predicts subsequent cancer therapy–related cardiac dysfunction in patients with breast cancer treated by epirubicin-based chemotherapy or left-sided RT. Eur Radiol 2022;32:1853–65. https://doi.org/10.1007/s00330-021-08260-7.

[23] Roujol S, Weingärtner S, Foppa M, Chow K, Kawaji K, Ngo LH, et al. Accuracy, precision, and reproducibility of four T1 mapping sequences: a head-to-head comparison of MOLLI, ShMOLLI, SASHA, and SAPPHIRE. Radiology 2014;272:683–9. https://doi.org/10.1148/radiol.14140296.

[24] Huang L, Neji R, Nazir MS, Whitaker J, Reid F, Bosio F, et al. Fast myocardial T1 mapping using shortened inversion recovery based schemes. J Magn Reson Imaging 2019;50:641–54. https://doi.org/10.1002/jmri.26649.

[25] Le JV, Mendes JK, McKibben N, Wilson BD, Ibrahim M, DiBella EVR, et al. Accelerated cardiac T1 mapping with recurrent networks and cyclic, model-based loss. Med Phys 2022;49:6986–7000. https://doi.org/10.1002/mp.15801.

[26] Yu C-Y, Huang T-Y, Chung H-W. Single breath-hold MR T1 mapping in the heart: hybrid MOLLI combining saturation and inversion recovery. Magn Reson Imaging 2023;96:85–92. https://doi.org/10.1016/j.mri.2022.12.001.

[27] Milotta G, Bustin A, Jaubert O, Neji R, Prieto C, Botnar RM. 3D whole-heart isotropic-resolution motion-compensated joint T1/T2 mapping and water/fat imaging. Magn Reson Med 2020;84:3009–26. https://doi.org/10.1002/mrm.28330.

[28] Qi H, Bustin A, Cruz G, Jaubert O, Chen H, Botnar RM, et al. Free-running simultaneous myocardial T1/T2 mapping and cine imaging with 3D whole-heart coverage and isotropic spatial resolution. Magn Reson Imaging 2019;63:159–69. https://doi.org/10.1016/j.mri.2019.08.008.

[29] Christodoulou AG, Shaw JL, Nguyen C, Yang Q, Xie Y, Wang N, et al. Magnetic resonance multitasking for motion-resolved quantitative cardiovascular imaging. Nat Biomed Eng 2018;2:215–26. https://doi.org/10.1038/s41551-018-0217-y.

[30] Hamilton JI, Jiang Y, Chen Y, Ma D, Lo W-C, Griswold M, et al. MR fingerprinting for rapid quantification of myocardial T1, T2, and proton spin density. Magn Reson Med 2017;77:1446–58. https://doi.org/10.1002/mrm.26216.

[31] Kellman P, Hansen MS. T1-mapping in the heart: accuracy and precision. J Cardiovasc Magn Reson 2014;16:2. https://doi.org/10.1186/1532-429X-16-2.

[32] Kellman P, Xue H, Chow K, Howard J, Chacko L, Cole G, et al. Bright-blood and dark-blood phase sensitive inversion recovery late gadolinium enhancement and T1 and T2 maps in a single free-breathing scan: an all-in-one approach.

J Cardiovasc Magn Reson 2021;23:126. https://doi.org/10.1186/s12968-021-00823-3.

[33] Keijnemans K, Borman PTS, Raaymakers BW, Fast MF. Effectiveness of visual biofeedback–guided respiratory-correlated 4D-MRI for radiotherapy guidance on the MR -linac. Magn Reson Med 2024;91:297–311. https://doi.org/10.1002/mrm.29857.

[34] Pavon AG, Porretta AP, Arangalage D, Domenichini G, Rutz T, Hugelshofer S, et al. Feasibility of adenosine stress cardiovascular magnetic resonance perfusion imaging in patients with MR-conditional transvenous permanent pacemakers and defibrillators. J Cardiovasc Magn Reson 2022;24:9. https://doi.org/10.1186/s12968-021-00842-0.

[35] Bangerter NK, Hargreaves BA, Vasanawala SS, Pauly JM, Gold GE, Nishimura DG. Analysis of multiple-acquisition SSFP. Magn Reson Med 2004;51:1038–47. https://doi.org/10.1002/mrm.20052.

[36] Roeloffs V, Rosenzweig S, Holme HCM, Uecker M, Frahm J. Frequency-modulated SSFP with radial sampling and subspace reconstruction: a time-efficient alternative to phase-cycled bSSFP. Magn Reson Med 2019;81:1566–79. https://doi.org/10.1002/mrm.27505.

[37] Slawig A, Wech T, Ratz V, Tran-Gia J, Neubauer H, Bley T, et al. Multifrequency reconstruction for frequency-modulated b SSFP. Magn Reson Med 2017;78:2226–35. https://doi.org/10.1002/mrm.26630.

[38] Kim KH, Park S-H. Artificial neural network for suppression of banding artifacts in balanced steady-state free precession MRI. Magn Reson Imaging 2017;37:139–46. https://doi.org/10.1016/j.mri.2016.11.020.